DTU Library

Cross-borehole DCIP monitoring of ZVI in-situ distribution. Hvedemarken 3-5, Farum

Lévy, Léa; Thalund-Hansen, Rasmus; Bording, Thue; Vest Christiansen, Anders; Bjerg, Poul L.

Publication date:
2023

Document Version
Publisher's PDF, also known as Version of record

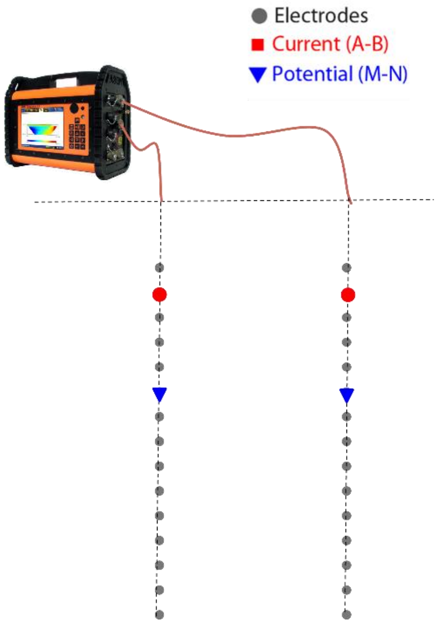

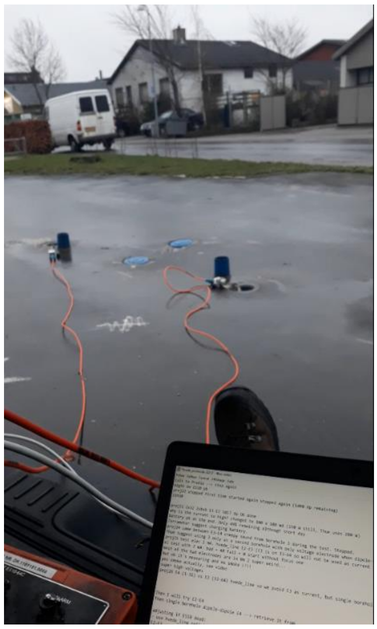

Cross-borehole DCIP monitoring of ZVI in-situ distribution. Hvedemarken 3-5, Farum

Léa Lévy[a], Rasmus Thalund-Hansen[b], Thue Bording[c], Anders Vest Christiansen[c], Poul L. Bjerg[b]

a) Lund University, Lund, Sweden *)

b) Department of Environmental and Resource Engineering, Technical University of Denmark, DTU, 2800 Kgs. Lyngby, Denmark.

c) Department of Geoscience, Aarhus University, 8000 Aarhus C, Denmark.

*) Formerly at HydroGeophysics Group, Department of Geoscience, Aarhus University, Denmark.

June 2023

TABLE OF CONTENTS

1. BACKGROUND AND GENERAL SETTING

Introduction

This report assesses the application of cross-borehole ERT at a pilot scale test site undergoing remediation by injection of reactive reagents to remove chlorinated ethenes. The pilot scale test site, the design, result and recommendation with respect to the remediation are reported in Region Hovedstaden (2023).

This report describes the use of cross-borehole DCIP (direct current – induced polarization) for monitoring the injection pilot scale remediation at Hvedemarken. The report describes three aspects:

- Monitoring the injection by use of DCIP data
- Determination of hydraulic conductivity (K) from DCIP data
- Quantification of Contaminant Mass Discharge (CMD)

The main focus will be on the monitoring of the remediation reagents which was the original focus of the project.

A scientific paper describing in more details the methods and results is published in Water Resources Research [*Lévy et al.20022*]. A second paper focusing on hydraulic conductivity and contaminant mass discharge is currently under revision [Thalund-Hansen *et al.*, 2023]. A note describing the application of the contaminant mass discharge at the site is included as an appendix in Region Hovedstaden (2023). Finally, a paper describing the biogeochemical processes and potential relationship to DCIP is under preparation [Thalund-Hansen *et al.*, in prep].

The pilot scale test, setting and injection

The pilot scale test site is located on a private and paved parking lot with a complex infrastructure including electricity cables, pipes, and drainage systems. The shallow subsurface is dominated by Quaternary sediments (Fig. 1c). A 10-meter section of the subsurface, entirely below the water table, is investigated here: from 10 to 20 m below ground surface (mbgs), corresponding to 29 to 19 m above sea level (masl). Three main geological layers were identified by borehole logs and sediment sample analyses: (i) glacial clayey till above the section investigated (ii) sandy till in the upper part of the investigated section and (iii) glacio-fluvial meltwater sand in the lower part (Fig. 1c). Preliminary geological investigations show that the transition between the sandy till and meltwater sands occurs between 13 and 14.5 mbgs.

The site hosted a packaging and plastic factory in the period 1959-1989. Several hot spots with groundwater contamination have been identified in the source area, mainly chlorinated solvents and petroleum hydrocarbons. The treatment zone in this experiment is located in the contaminant plume, 50 m down-gradient of the source (Fig. 1b).

The anti-methanogenic chemical reduction agent Provect-IR® was chosen as a remediation agent. It was injected along with the non-pathogenic bacterial culture KB-1®. Provect-IR® consists of a micro-scale ZVI, calcium dipropionate, yeast extracts, guar gum and sodium sulfite.

The contaminant plume in the treatment zone consists mainly of chlorinated ethenes (TCE, cis-DCE). The injection initiates reductive dechlorination where TCE through a sequential pathway is reduced to harmless ethene and ethane. The dechlorination process requires spreading of the injectant including ZVI, electron donors and the KB-1® culture.

A first injection campaign took place in August 2019 in seven injection wells, with ten injection points each (red dots on Fig. 1d). Several daylighting events (transport of ZVI up to the surface) were witnessed during the injection and may have created upstream passages. A second injection campaign took place in December 2020 in 14 injection wells, with injection points in the depth-range 13-17 m (location shown in Fig. 2).

This report describes the use of cross-borehole DCIP (direct current – induced polarization) for monitoring the injection pilot scale remediation at Hvedemarken. The report describes three aspects:

- Monitoring the injection by use of DCIP data
- Determination of hydraulic conductivity (K) from DCIP data
- Quantification of Contaminant Mass Discharge (CMD)

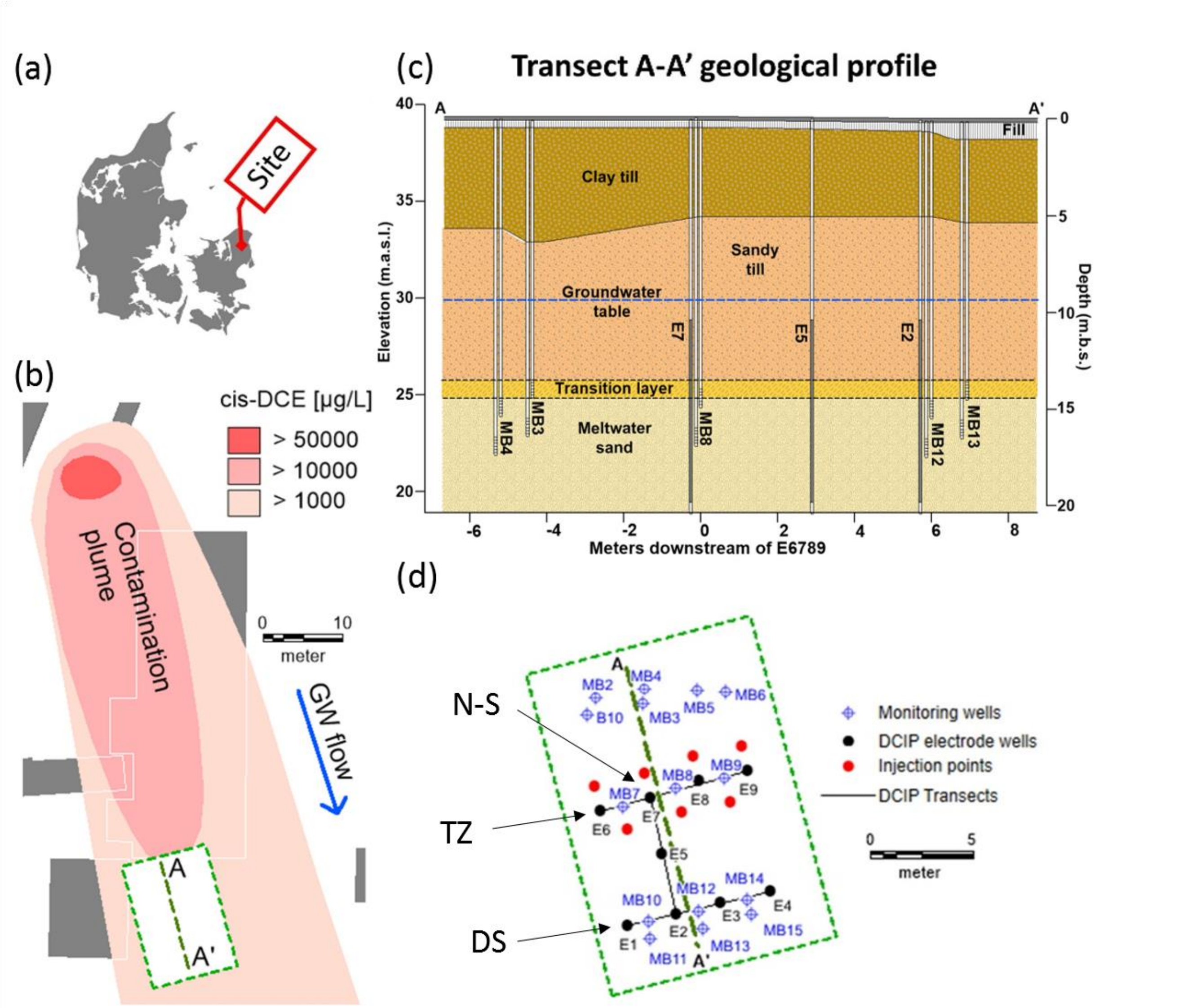

Figure 1. Presentation of the site. (a) Map of Denmark, with site location highlighted. (b) Zoom on test site showing the contamination plume, buildings (grey boxes) and target area (green rectangle). (c) Geological transect oriented N-S showing three electrode boreholes "EX" and five monitoring wells "MBXX". Note that the cross-borehole experiment takes place below the groundwater table. (d) Zoom on the target area showing electrode boreholes, injection points and monitoring wells. Note that injection points are located upstream (north) and downstream (south) of the transect E6-E7-E8-E9.

The main focus is the monitoring of the remediation reagents, which was the original focus of the project.

A scientific paper describing in more details the methods and results is published in Water Resources Research [*Lévy et al.20022*]. A second paper focusing on hydraulic conductivity and contaminant mass discharge is currently under revision [Thalund-Hansen *et al.*, 2023]. A note describing the application of the contaminant mass discharge at the site is included as an appendix in Region Hovedstaden (2023). Finally, a paper describing the biogeochemical processes and potential relationship to DCIP is under preparation [Thalund-Hansen *et al.*, in prep].

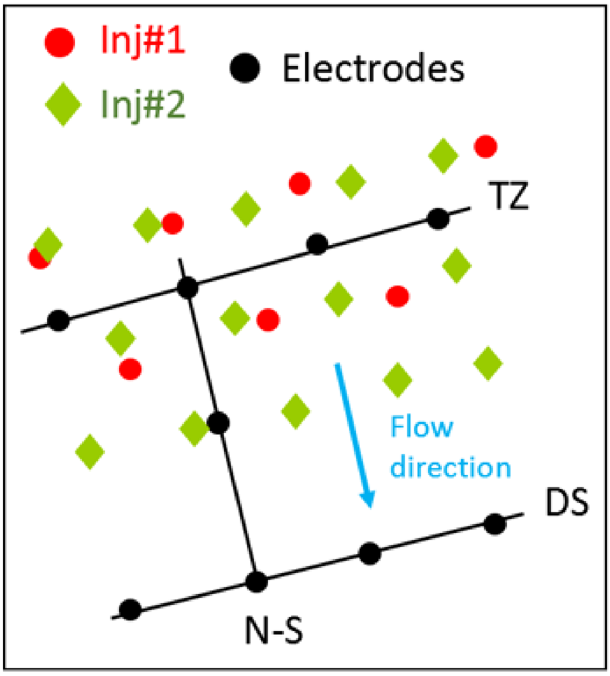

Figure 2. Simplified map of the three transects and injection screens.

2. MOTIVATION FOR DCIP MONITORING

Successful delivery into the subsurface is very challenging for all injection methods [*Phenrat et al.*, 2009]. Rapid assessment of reagent distribution is crucial to determine whether sufficient contact between the contaminated aquifer and reagents took place, because we can react and plan a re-injection shortly after or change the injection strategy. In the context of Hvedemarken pilot site, the injection of a viscous slurry of ZVI particles in subsurface systems of intermediate hydraulic conductivity (5.10^{-7} – 5.10^{-5} m/s) presents a series of challenges, such as complex water chemistry, geological heterogeneities and unintentional preferential pathways [*Velimirovic et al.*, 2014].

Electrical resistivity tomography (ERT) imaging has the potential to provide a rapid, spatially continuous and well-resolved assessment of the reagent distribution, using the electrical signature of remedial amendments [*LaBrecque et al.*, 1996; *Singha and Gorelick*, 2005; *Slater et al.*, 2002]. Induced polarization (IP) tomography senses the ability of the subsurface to temporarily store electric charges and thus has the potential to detect electrically chargeable ZVI particles [*Joyce et al.*, 2012; *Shi et al.*, 2015; *Slater et al.*, 2005]. An added-benefit is that it can help evaluate hydraulic conductivity [e.g., *Binley et al.*, 2016; *Fiandaca et al.*, 2018b; *Weller et al.*, 2015]. Recent studies show encouraging results for monitoring the injection of ZVI reagents with surface time-lapse ERT/IP [*Flores Orozco et al.*, 2019; *Flores Orozco et al.*, 2015; *Nivorlis et al.*, 2021]. The term DCIP indicates that ERT (direct current, hence "DC") and IP are combined. The conduction and polarization properties of the subsurface, measured by the DCIP method, can reflect parameters such as iron content, hydraulic conductivity and changes in pore water chemistry (Table 1).

Relation between DCIP and chemical compounds of interest

In an electrical context, geological formations can be thought of as a combination of resistors and capacitors. Ions in pore water and those connected to clay minerals are charge carriers in aquifers. Conductive water and clay minerals can be represented by conductors with high electrical conductivity, as opposed to freshwater and pure quartz sand or gravel, which have lower electrical conductivity. In the absence of clay minerals and metallic particles, the electrical charge carriers are predominantly ions in pore water. In this case, the total aquifer electrical conductivity, also called "formation conductivity", is proportional to the electrical conductivity of pore water, “water EC”, and thus to the concentration of major ions [*Archie*, 1942; *Maurya et al.*, 2018b].

In the Hvedemarken remediation experiment, four ions mainly contribute to changes in water EC (Fig. 3): dissolved iron Fe(diss), calcium (Ca^{2+}), hydrogen carbonate (HCO_3^-) and chloride (Cl^-). The three first ions are either present in the injected reagent or released upon reaction with the surrounding aquifer. They represent, together with other compounds such as non-volatile organic carbon (NVOC), what we call the “remediation cloud”. Due to their influence on the water EC, their variations can be captured by DCIP, although the respective variations of each ion cannot be distinguished. The NVOC acts as an electron donor and stimulates iron reduction, sulfate reduction and methanogenesis. This will generate dissolved iron, formation of hydrogen carbonate and precipitates like calcium carbonate, siderite ($FeCO_3$ and iron sulfides (FeS, FeS_2). NVOC will not, as a non-charged species, give an EC signal.

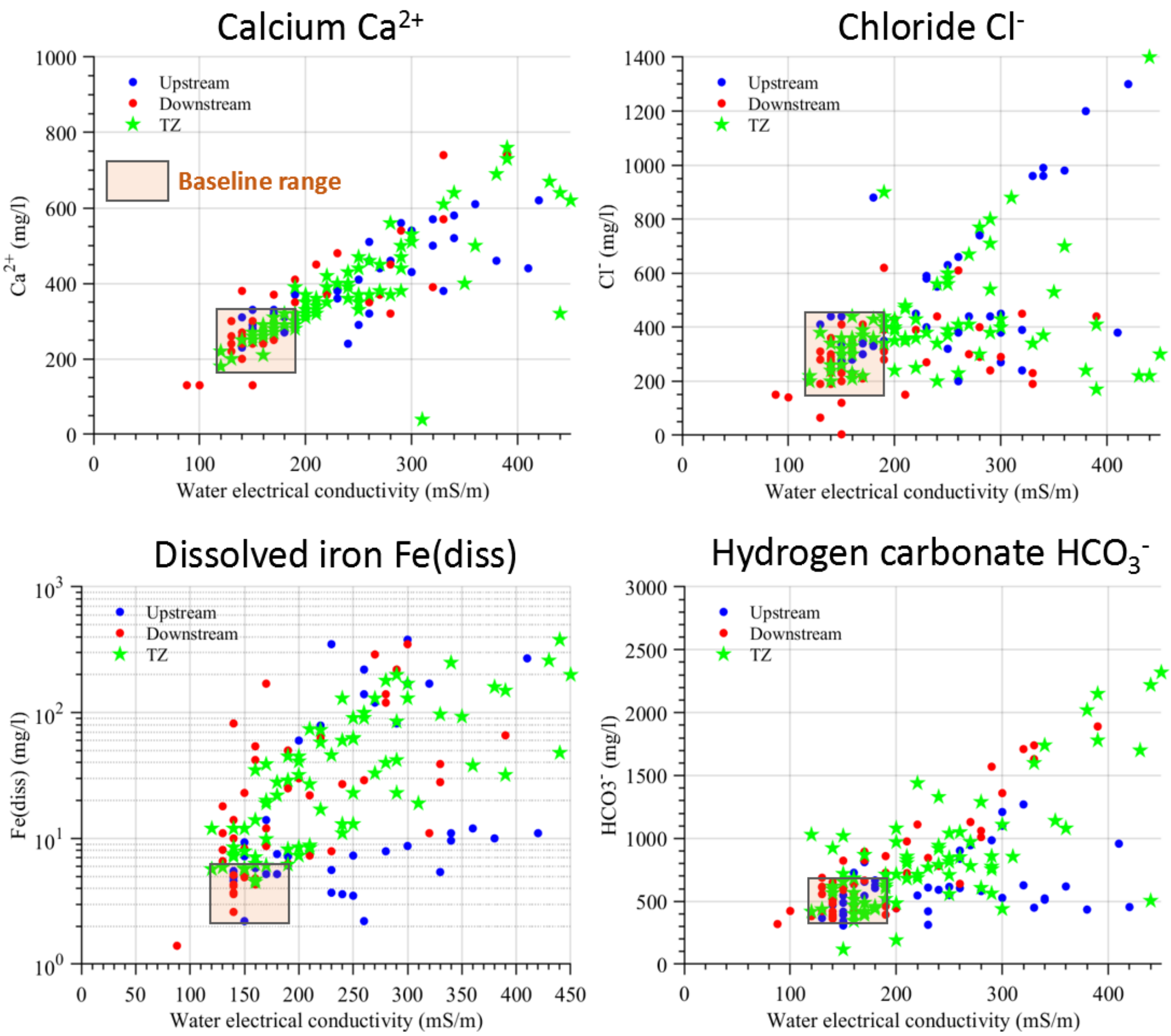

Figure 3. Correlation between water EC and concentration of four ionic compounds of interest for monitoring the injection and remediation: $Ca2^+$, Cl^-, Fe(diss), HCO_3^- concentration. Data are measured using groundwater samples from monitoring wells. All available data are plotted together (all wells, all monitoring dates). Note that Fe(diss) concentrations are represented with a logarithmic scale.

The contamination consists mainly of chlorinated ethenes (TCE, cis-DCE), which are uncharged. The injection initiates reductive dechlorination, however, the reductive dechlorination cannot be monitored by the DCIP method. The DCIP method can monitor the injection cloud and the outcome of the processes induced by the injectant, but not the production of lower chlorinated ethenes nor the production of ethane and ethane.

All interfaces favor the accumulation of ions, e.g., between pore water and sediment matrix, which is similar to the effect of a capacitor in an electronic circuit and is called polarization. The larger the total pore surface area, the more charge accumulation is possible [*Weller and Slater*, 2019]. Semi-conducting metallic particles (e.g., pyrite or zero-valent iron) also cause electronic conduction and polarization. Polarization caused by semi-conductor is usually several orders of magnitude stronger than sediment/water interfaces, due to the possibility of electron redistribution within their crystal structure [see e.g. *Revil et al.*, 2017; *Slater et al.*, 2005; *Slater et al.*, 2006].

The wide range of geological and chemical features that affect the electrical signal is the main strength and the main limit of the method, due to non-unique interpretation of geophysical signals (Table 1).

Table 1. Principle of the DCIP method: physical processes proposed by the scientific community, parameters measured and corresponding environmental parameter with potential applications. The last column gives a non-exhaustive reference list for further information on the processes and the conversion from DCIP to environmental parameters. DCIP parameters are: resistivity ρ, real conductivity σ', imaginary conductivity σ'', maximum phase angle Φ_{max}, relaxation time τ and Cole-Cole exponent C.

Physical process	Electric charge carrier	DCIP param.	Environmental param.	Possible environmental applications	References
Electrolytic conduction	Ions in pore water	ρ or σ'	Equivalent ion concentration	Mapping contamination. Monitoring distribution of reagent.	[*Archie*, 1942; *Balbarini et al.*, 2018; *Maurya et al.*, 2018a]
Surface + interfoliar conduction	Ions in clay minerals	ρ or σ'	Cation Exchange Capacity	Mapping clay caps (volcanic). Mapping lithological contrasts, e.g. clay layers.	[*Lévy et al.*, 2018; *Waxman and Smits*, 1968]
Electronic conduction	Electrons in connected metallic minerals	ρ or σ'	Volume of metallic particles	Mapping and monitoring distribution of large metallic clusters (sulphides, solid iron).	[*Pridmore and Shuey*, 1976; *Shuey*, 1975; *Slater et al.*, 2006]
Ionic polarization	Ions adsorbed at solid surface and in pore water	Φ_{max} or σ''	Pore surface area	Mapping hydraulic conductivity.	[*Bücker and Hördt*, 2013; *Fiandaca et al.*, 2018b; *Weller et al.*, 2015]
Electronic polarization	Electrons in disseminated metallic minerals	Φ_{max}	Volume of metallic particles	Mapping/monitoring distribution of disseminated metallic particles.	[*Lévy et al.*, 2019a; *Pelton et al.*, 1978; *Slater et al.*, 2005]
		τ, C	Grain size of metallic particles		

Relation between DCIP and hydraulic conductivity

In sedimentary contexts, the amplitude of polarization created by the application of an electric field in the aquifer can be translated into hydraulic conductivity, provided that several conditions are met [*Robinson et al.*, 2018; *Weller and Slater*, 2019; *Weller et al.*, 2015]. Situations where hydraulic conductivity calculation from DCIP is not possible include very conductive environments (e.g. in highly altered faciès where smectite is dominant or in saltwater-dominated aquifers), where the voltage signal level becomes too low [*Lévy et al.*, 2019b], as well as environments with metallic particles, as they strongly contribute to the polarization signal [*Lévy et al.*, 2019a]. Note that hydraulic conductivity field estimated with polarization measurements represents the bulk "matrix" conductivity (i.e. not considering the effect of narrow flow paths). The hydraulic conductivity is estimated in the aquifer before the injection. Determination of the hydraulic conductivity from DCIP after the injection would be affected by the ZVI and precipitates.

3. THE CROSS-BOREHOLE DCIP METHOD

ERT consists of injecting a direct current (DC) through two current electrodes (A and B) and measuring the resulting voltage at two potential electrodes (M and N, see illustration in Fig. 4). The time-domain induced polarization (TDIP) method consists of recording the same voltage signal *V(t)* but with a high sampling rate. The ERT and TDIP methods are carried out with the same instrument at the same time, which we call here the "DCIP" method.

Advantage of the cross-borehole set-up

Surface DCIP imposes a trade-off between spatial resolution and depth of investigation, due to the attenuation of current injected from the surface. This is particularly problematic at the Hvedemarken pilot site, where the target volume is below 10 m depth and where limited space is available to lay out surface cables due to dense infrastructure. In addition, the concrete cover and presence of buried infrastructure at shallow levels (drainage and drinking water pipes, power cables) in this urban area negatively impacts the data quality when electrodes are at the surface [see e.g. *Nivorlis et al.*, 2019].

Data quality, spatial resolution and sensitivity for deep targets can improve dramatically when electrodes are installed in boreholes [*Daily and Ramirez*, 1995]. Cross-borehole ERT has been successfully used to monitor the migration of saline tracers in well-controlled tank experiments [*Slater et al.*, 2002] and in the field [*Singha and Gorelick*, 2005]. It has also been installed at contaminated sites to monitor groundwater changes related to in-situ remediation [*Bording et al.*, 2021; *Nivorlis et al.*, 2019]. The term cross-borehole means that electrodes are in boreholes, buried under the surface, as opposed to installed at the surface. Three types of electrode configurations are used in this study as sketched in Fig. 4:

1. "Single borehole": all four electrodes are in the same borehole.
2. "AB-MN": the current electrodes (A and B) are in one borehole and the potential electrodes (M and N) in another borehole, and
3. "AM-BN": where current is sent between two boreholes and voltage measured between the two same boreholes [*Bing and Greenhalgh*, 2001; *Bording et al.*, 2019].

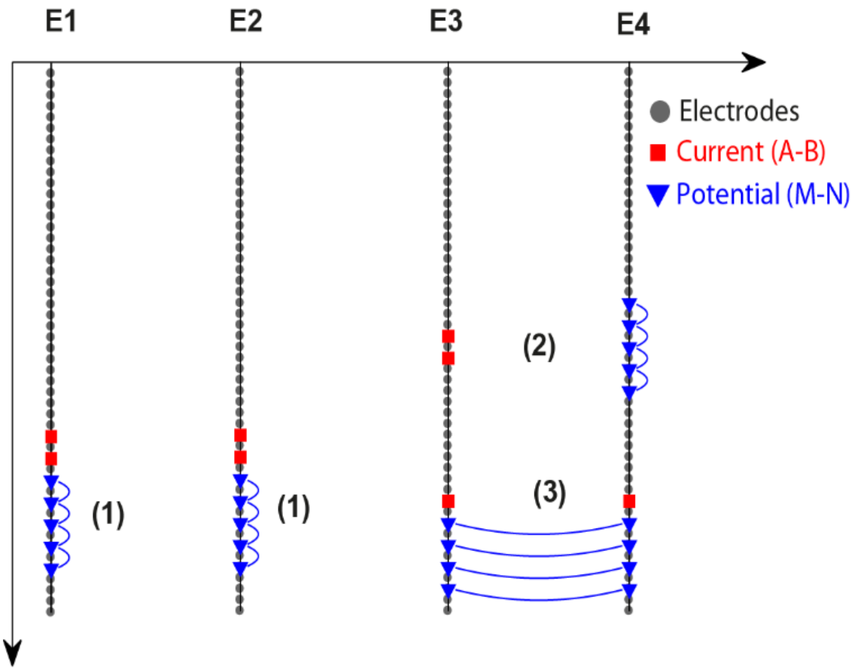

Figure 4. Three cross-borehole electrode configurations used in this study: (1) single borehole; (2) "AB-MN"; (3) "AM-BN".

Cross-borehole DCIP data acquisition

Nine boreholes were installed in June 2019, with 32 stainless steel ring electrodes in each. The electrodes are mounted on 32 mm PVC tubes from ROTEK (see hand drawing from the production process in Fig. 7). The distance between neighboring boreholes is in the range 2.5-3 m, and the vertical spacing between electrodes is 0.3 m between electrodes. All electrodes are installed in the depth range 10-20 m.

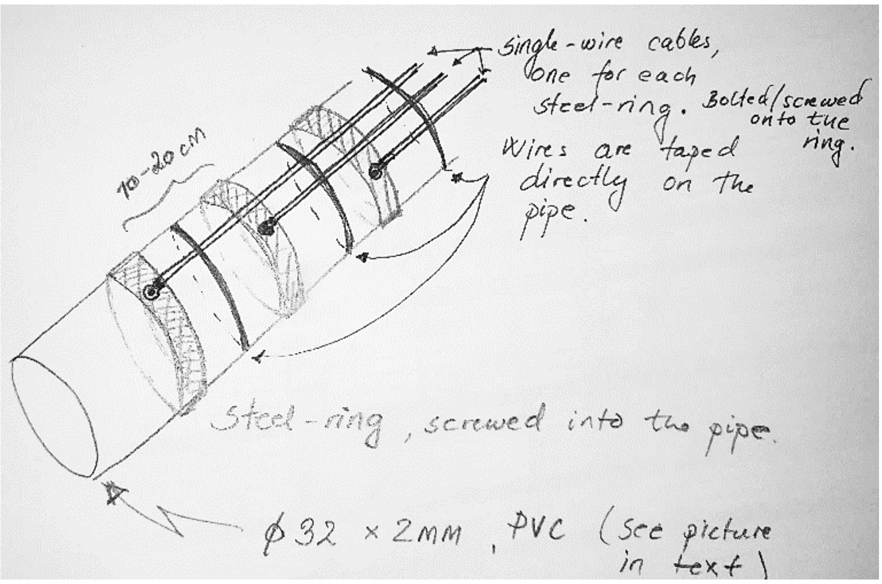

Figure 7. Schematic drawing of the electrode tubes used for the production process.

Ten rounds (R1 to R10) of cross-borehole DCIP acquisitions were carried out, including three before injection of reagent (Table 2). Technical issues occurred at R2 and R6 and therefore little to no data were available at these rounds.

Table 2. Overview of geophysical data acquisition and chemical sampling. The double thick line indicates the injections (27-29/08/2019 and 20-22/12/2020). Available good quality DCIP data at the three transects are marked with GQ. Available DCIP data with degraded quality are marked with DQ.

Round	Date	Days	TZ transect	N-S transect	Downstream transect	Water sampling	Extraction of sediment core
R1	15/07/2019	Baseline	GQ	GQ	GQ	X	-
R2	02/08/2019	Baseline	-	-	-	-	-
R3	08/08/2019	Baseline	GQ	GQ	GQ	-	-
R4	30/08/2019	Inj#1 + 1	GQ	GQ	GQ	-	X
R5	10/09/2019	Inj#1 + 14	GQ	GQ	GQ	X	-
R6	02/12/2019	Inj#1 + 90	GQ	-	-	X	-
R7	02/06/2020	Inj#1 + 270	GQ	GQ	-	X	-
R8	01/12/2020	Inj#1 + 450 (new bas.)	GQ	GQ	-	X	-
R9	15/01/2021	Inj#2 + 22	DQ	DQ	-	X	-
R10	20/09/2021	Inj#2 + 240	DQ	DQ	-	X	-

Data representation

For each ABMN quadrupole, the apparent resistivity, ρ_a, is calculated by Equation 1 based on the measured potential and geometric configuration:

$$\rho_a = \frac{4\pi}{\frac{1}{|AM|}-\frac{1}{|AN|}-\frac{1}{|BM|}+\frac{1}{|BN|}} \frac{\Delta V_{MN}}{I_{AB}} \tag{1}$$

where I_{AB} is the current injected between electrodes A and B, ΔV_{MN} is the potential difference measured between electrodes M and N, and |AM|, |AN|, |BM| and |BN| are the distances between electrodes.

A convenient way to display ERT measurements is a two-dimensional "pseudo-section" plot, which is obtained by placing each apparent resistivity measurement at a vertical and lateral focus point [Loke and Barker, 1996]. Each apparent resistivity measurement averages the resistivity of the subsurface within the influence area of the electrical current, which depends on the electrode configuration and the conductivity of the medium [Telford et al., 1990]. Examples of apparent resistivity pseudo-sections are shown in Fig. 5, for data measured at Hvedemarken.

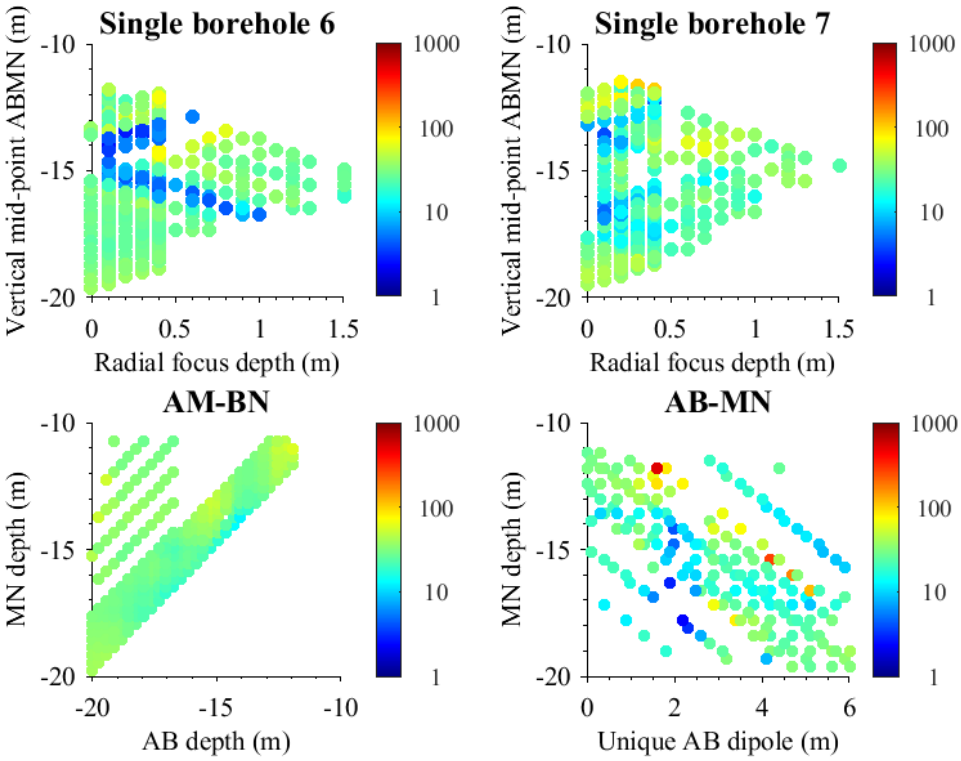

Figure 5. Resistivity pseudo-sections for cross-borehole acquisition between boreholes E6 and E7 1 day after injection. The four sections correspond to four types of acquisition: single borehole (in each borehole), cross-borehole type "AM-BN" and type "AB-MN".

For TDIP measurements, charge and discharge curves can be represented by the integral apparent chargeability $< M >$. It represents the area enclosed by the discharge curve, V(t), and its zero asymptote, in a given time-window, [t1:t2], divided by the primary voltage V_p and the time-window width as described by Equation 2 *[Bertin and Loeb, 1976; Sumner, 1976]*.

$$< M > = \frac{1}{t_2 - t_1} \int_{t_1}^{t_2} \frac{V(t)}{V_p} dt \tag{2}$$

Figure 6 shows a sample of IP discharge curves (data and forward shown in blue and pink, respectively), for different electrode configurations.

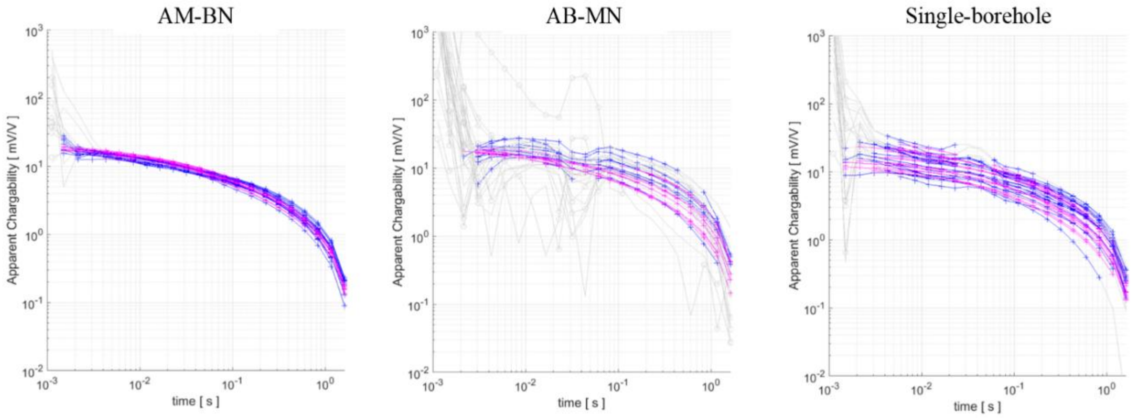

Figure 6. IP data and forward prediction (blue and pink curves, respectively) at selected locations. Left and central panels correspond to cross-borehole between E5 and E7. Right panel corresponds to single borehole in E5. All data are from R3 (baseline). The grey points and lines correspond to noisy data removed from the dataset before inversion.

Data processing and inversion

The data are first processed manually, where data points with apparent resistivity above 1000 Ωm and below 1 Ωm are removed. The interval 1-1000 Ωm was evaluated as a good indicator of decent data quality based on voltage signal quality and pseudo-section manual inspection.

In order to obtain resistivity and IP models of the subsurface, inversion is necessary. For that, data are combined into three 2D profiles: (i) E6-E7-E8-E9 (profile running West-East in the treatment zone, here-after called TZ transect), (ii) E7-E5-E2 (profile running North-South, parallel to the natural hydraulic gradient, here-after called N-S transect) and (iii) E1-E2-E3-E4 (profile parallel to the TZ transect, 7 m to the south, here-after called the Downstream "DS" transect). These profiles can be seen in Figs 1 and 2.

Inversion of resistivity and chargeability data was performed using AarhusInv. More information can be found in *Auken et al.* [2014] for inversion and in *Fiandaca et al.* [2013] for forward modelling of cross-borehole data and Jacobian computation. The specific borehole implementation (buried electrodes) is presented in *Bording et al.* [2019]. The forward response is calculated in 2.5D along a given profile, assuming that the 2D model extends indefinitely in the direction normal to the profile plane, and electrodes are modelled as points.

The model mesh for inversion is composed of 0.15 m x 0.5 m cells (thickness x width), corresponding to 28 model columns in each profile and 78 layers between the uppermost and bottom electrodes.

The parameters in each model cell are constrained to the neighboring cells in the vertical and horizontal directions.

In the model space, the frequency-dependent complex conductivity σ^* is described through a re-parameterization of the Cole-Cole model, the maximum phase angle (MPA) model, which give better-resolved parameters [*Cole and Cole*, 1941; *Fiandaca et al.*, 2018a]. The MPA model consists of four parameters: the resistivity ρ, the maximum phase angle ϕ_{max}, the relaxation time τ and the Cole-Cole exponent C. ϕ_{max} is particularly suited for emphasizing disseminated metallic particles [*Lévy et al.*, 2019a].

The so-called “time-lapse” inversion follows *Fiandaca et al.* [2015], in a cascaded inversion scheme. The starting model of the inversion is the final model of a reference round. The new model is constrained to the baseline model through the asymmetric minimum support norm. This time-lapse inversion scheme focus the time-lapse changes, retrieving the smallest model differences compatible with the data. On the other hand, with the so-called “stand-alone” inversion, no constraints to the starting model are imposed.

Estimations of hydraulic conductivity from DCIP

The hydraulic conductivity computation, presented in equation 4, relies on laboratory-based relationships established for unconsolidated sediments by *Weller et al.* [2013] and *Weller et al.* [2015], that link electrical properties and permeability.

$$K = \frac{\rho g}{\mu} \cdot 3.47 \cdot 10^{-16} \cdot \frac{\sigma_0^{1.11}}{\sigma''^{2.41}} \tag{4}$$

Where σ_0 is the real conductivity and σ'' the imaginary conductivity, calculated as $\sigma_0 = \frac{1}{\rho}$ and $\sigma'' = \frac{\Phi_{max}}{\rho}$. The permeability is further converted to hydraulic conductivity, using $\frac{\rho g}{\mu} = 7.7437 \cdot 10^4\ cm^{-1}.s^{-1}$, where ρ and μ are the density and viscosity of water at 11°C and g is the gravity acceleration. In practice, the K-distribution only weakly depends on salinity variations. Further details can be found in [*Bording et al.*, 2021] and *Fiandaca et al.* [2018b].

4. OUTCOMES

The main outcome of cross-borehole DCIP monitoring at Hvedemarken is that the time-lapse resistivity imaging provides a reliable image of the spreading of the injectant, the “remediation cloud”, after injection. It fills the gap between chemical monitoring screens and provides a spatial picture of the distribution. It should be noted that DCIP cannot distinguish between compounds injected or generated during the injection. In addition the uncharged contamination with chlorinated ethenes (PCE, TCE, DCE, VC) and the production of ethene and ethane cannot be identified by DCIP. In this respect the monitoring is expected to be supplementary to chemical analyses. Another interesting outcome is the mapping of hydraulic conductivity distributions before the start of injection. These data can improve estimations of contaminant mass discharge as discussed in Thalund-Hansen et al. (2023). The application of DCIP for long-term monitoring is another aspect of the method which might be useful (Thalund-Hansen et al., in prep; Kessouri et al. 2022).

Monitoring remediation cloud with cross-borehole resistivity

In this section we focus on the resistivity inversion stemming from the ERT method (without induced polarization). We present in Fig. 7 the standalone result for the TZ transect.

The resistivity contrasts show both an influence of the remediation cloud and the host geology.

To assess the remediation cloud distribution over time and to subtract the influence of geology on the conductivity contrasts, time-lapse ERT results are presented in Figs 8, 9 and 10, for the TZ, N-S and DS transects, respectively.

We use the ratio between post-injection conductivity and baseline conductivity (R3 is taken as the baseline round). The ratio representation chosen emphasizes in blue high-conductivity anomalies caused by the injection: a darker color corresponds to a larger conductivity increase. The left plots illustrates the natural variability of the ERT signal, using the ratio R1/R3 (two baseline rounds). The other plots dynamically show the spreading of the reagent. Some light variations are visible in the TZ transect between R1 and R3 and are attributed to data noise. In the rest of our analyses we focus on anomalies that have a significantly darker color.

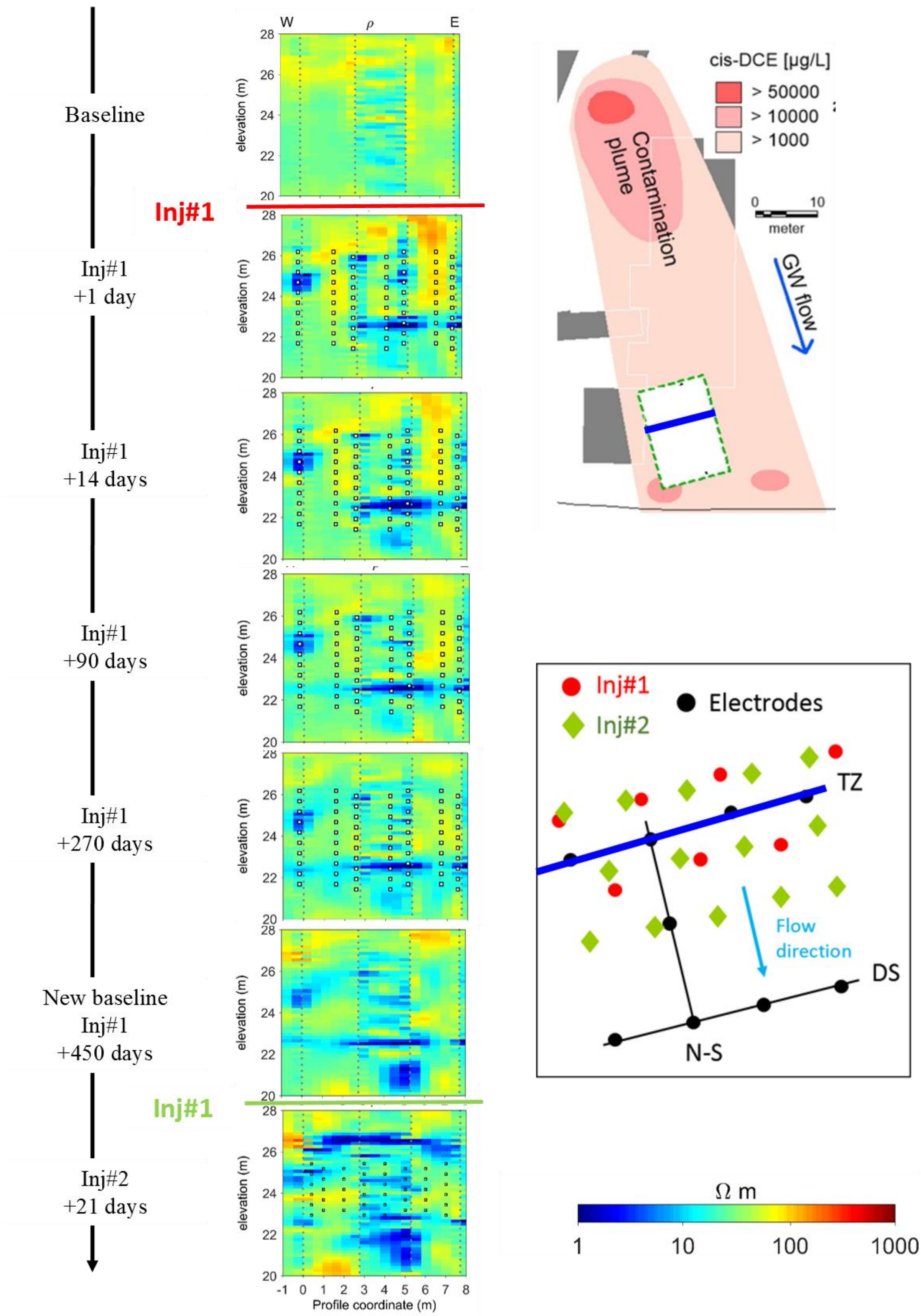

Figure 7. Standalone resistivity inversion results for the TZ transect at the baseline and six of the monitoring rounds.

Treatment Zone (TZ) transect

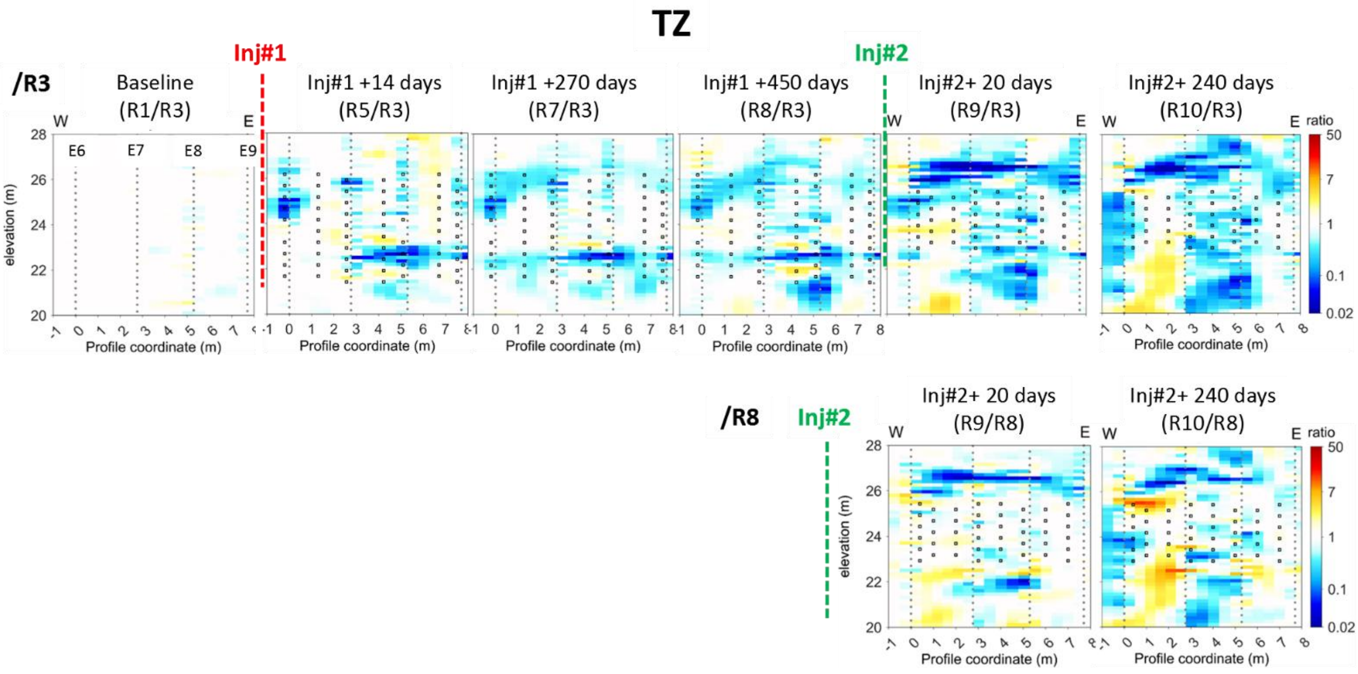

Figure 8. Cross-borehole resistivity ratio plots based on ERT inversion results in the TZ transect. The injection screens are shown as black squares. Note the different position for the rounds of injections. The top row shows ratios to the initial baseline R3, while the bottom row shows the ratio to the new baseline, R8, in order to emphasize the changes related to the second injection.

North-South (N-S) transect

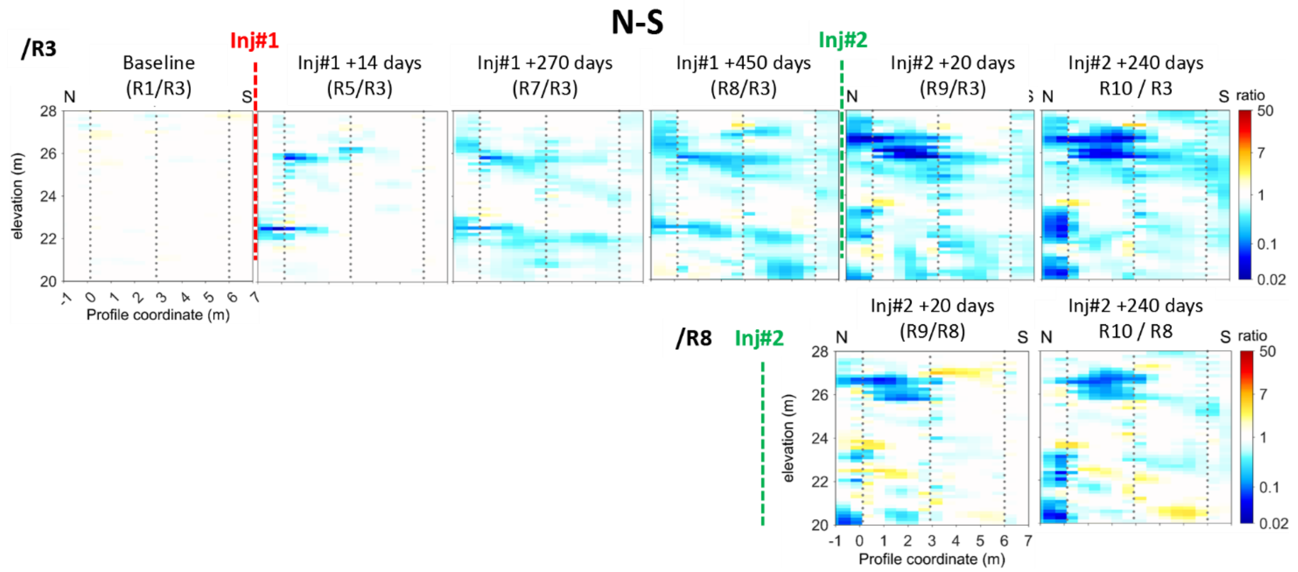

Figure 9. Cross-borehole resistivity ratio plots based on DC inversion results in the N-S transect. The top row shows ratios to the initial baseline R3, while the bottom row shows the ratio to the new baseline, R8, in order to emphasize the changes related to the second injection.

Downstream (DS) transect

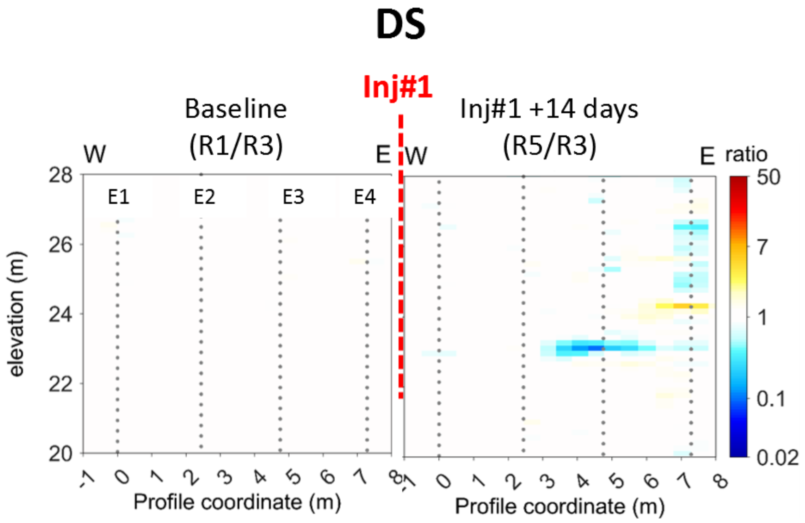

Figure 10. Cross-borehole resistivity ratio plots, based on DC inversion results in the DS transect. No data was available after R5 at this transect.

Qualitative comparison to chemical monitoring

Qualitatively, cross-borehole ERT and water chemistry compare well on the TZ, N-S, and DS transects (Fig. 11). In particular, limited spreading of the reagent at 23-25 masl is confirmed by chemical monitoring both on the TZ and N-S transects. The increased concentration of Fe(diss) at R5 in screen MB13-1 matches exactly the conductive anomaly inferred from ERT on the DS transect. However, this chemical increase is not reflected on the N-S transect. Note that screens projected on the N-S transect are up to 2 m away from the transect plane and thus local anomalies might not be captured.

In the N-S transect, no geophysical data are available north of E7, but monitoring screens show a clear increase of chemical compounds related to the reagent, especially at 22 masl.

The resolution of the cross-borehole ERT is very high compared to traditional analyses of water samples from monitoring screens. Thus the spatial patterns identified in the cross sections by cross-borehole ERT is not fully reflected in the traditional monitoring.

Sediment coring was also carried out shortly after the injection. Sediment extractions and magnetic susceptibility measurements identified distinct zones with high iron content. The locations were associated with clear magnetic susceptibility anomalies and correspond to the three main pieces of conductive cloud imaged by R5 and R6 (Figure 7 and 8).

Overall, the monitoring screens and cross-borehole ERT show consistent remediation cloud locations. Yet, the 2D anomalies observed with ERT provide a more complete image of the remediation cloud distribution than if based solely on monitoring screens.

Later in the field trial depth specific water sampling was performed with a Geoprobe rig was performed. These data provided information which to a higher degree matched the resolution of the cross-borehole ERT (see all data in Region Hovedstaden 2023). In future the development of the cross-borehole ERT it is advised to do include level specific water sampling in parallel with the geophysical measurements

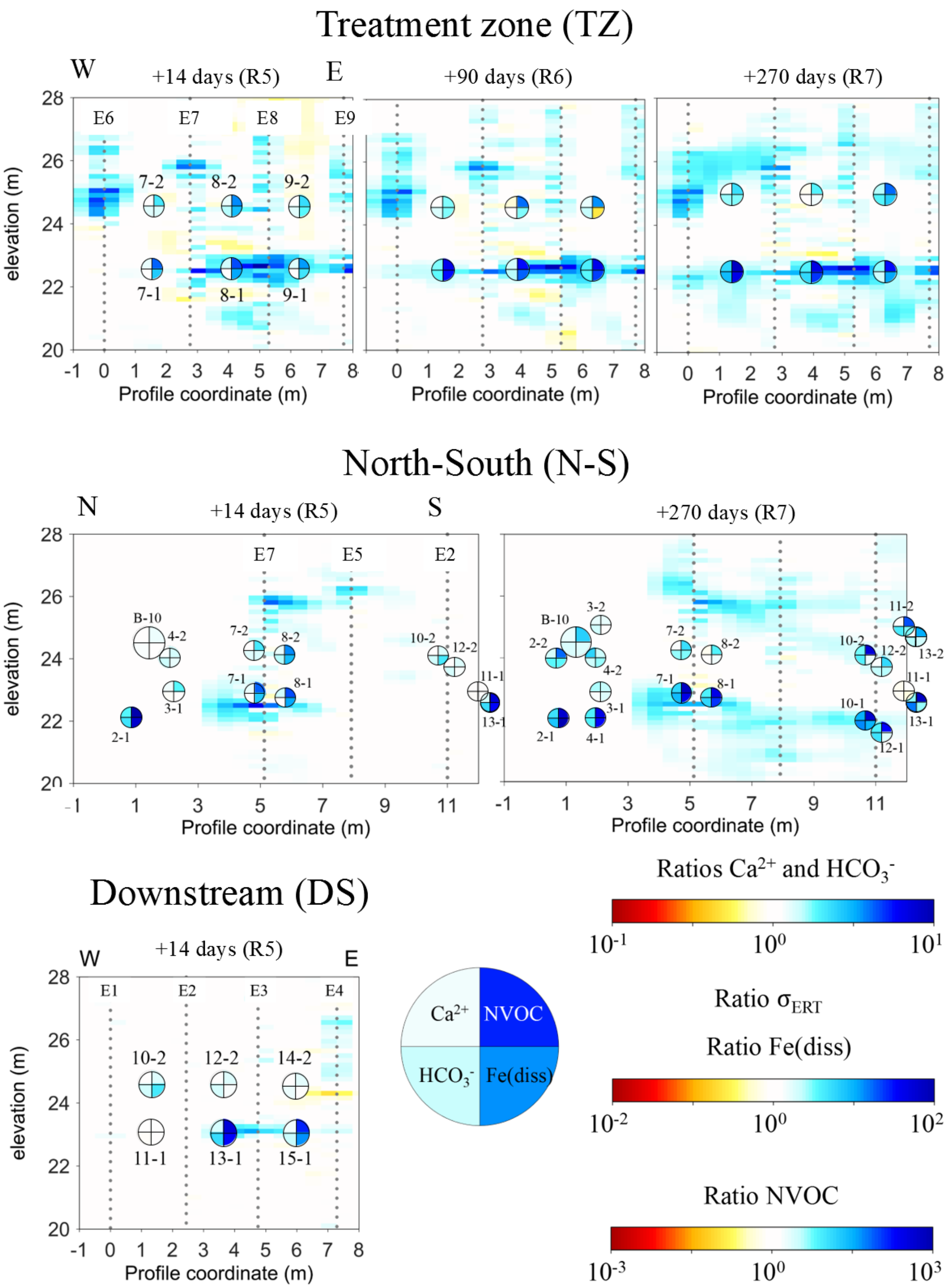

Figure 11. Comparison of electrical conductivity ratios obtained by time-lapse ERT (σ_{ERT}) to concentration ratios of calcium (Ca^{2+}), hydrogen carbonate (HCO_3^-), dissolved iron Fe(diss) and Non-Volatile Organic Carbon (NVOC) obtained by chemical monitoring. On the N-S transect, all screens projected are 1-2 m away from the figure plane. This is represented by a slight vertical shift (up for west of the plane and down for east). Most screens cover in reality a 1 m depth range (2 m for B-10). Relevant ID for electrode boreholes and monitoring screens are shown. Three different color scales covering increasing ratio range width: (i) Ca^{2+} and HCO_3^- (ii) σ_{ERT} and Fe(diss), (iii) NVOC.

K-field from DCIP and comparison with other K-methods

As described previously, cross-borehole DCIP can be used to estimate the hydraulic conductivities before injection. The formula is based on a laboratory-based relationship established for unconsolidated sediments. In addition, 18 slug tests and 31 grain size distribution analyses (GSA) from the control planes, were used for K-estimation. The comprehensive hydraulic conductivity data set with different methods allowed for a comparison between the DCIP derived hydraulic conductivity, slug test and K estimations from grain size distributions of sediment samples (Figure 12). Hydraulic conductivity is observed to be lower in the top sandy till layer than in the bottom meltwater sand. The full analyses of these data and the comparison between the methods are described in Thalund-Hansen et al. (2023). The the different methods showed an overall good agreement. The geometric mean of the hydraulic conductivities are very similar for all three K-methods, in the sandy till, in the meltwater sand and over the entire depth. In particular when it is recalled that studied K-estimation methods work on a very different scale in terms of radius of influence, sampling size and screen length, In addition they operate with different distances between sampling/testing points and they derive the K-values in different ways.

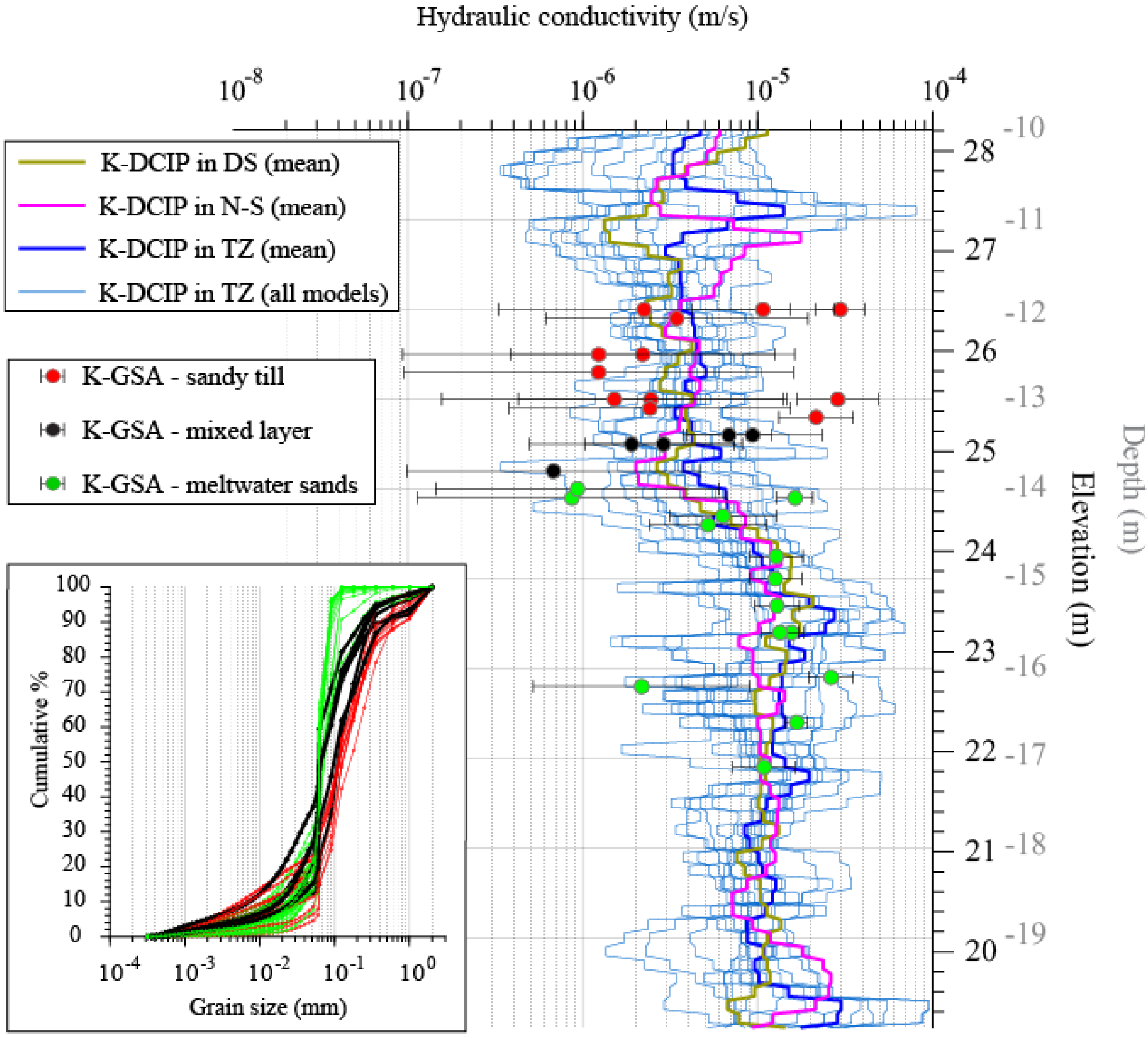

Figure 12. One-dimensional representation of the hydraulic conductivity field, based on estimations from DCIP inversions and grain size analyses (GSA). All vertical models are shown for the TZ transect (thin blue line), and the mean is shown for all three transects (three thicker lines). Both elevation and depth scales are shown, in black and grey, respectively. K-estimations based on GSA are represented by filled circles with error bars. The GSA themselves are represented as cumulative percentage, using the same color code, and illustrate a sharp transition at 25.4-25.8 m. The GSA plot includes analyses for 31 sediments samples coming from four boreholes in the TZ.

Interpreting injection pathways in light of the hydraulic conductivity distribution

The baseline situation of this experiment meets the requirements for hydraulic conductivity calculation from DCIP data: sedimentary context with relatively low and spatially-uniform ionic conductivity, no metallic particles, and little to no clay minerals. An advantage of K-DCIP estimations over point-sampling is that it provides a spatial picture of the permeability distribution with a much larger and coherent dataset, without significant bias due to local heterogeneity or spatial inconsistencies.

Using baseline DCIP data, we observe two distinct ranges of *K* values (Fig. 11): 10^{-7}-$5\cdot10^{-6}$ m/s in the upper part and $5\cdot10^{-6}$-10^{-4} m/s in the lower part, with a transition at around 25.5 masl.

In order to assess the reliability of these DCIP-based hydraulic conductivity predictions “K-DCIP”, we compare *K* evaluated from grain size analyses (K-GSA) to K-DCIP (Fig. 12). K-GSA estimations confirm the trend of lower hydraulic conductivity in the upper part versus higher hydraulic conductivity in the bottom part, with a transition at 25-25.5 masl. A few outliers are found with higher K-GSA values in the upper parts (e.g. at 26-27 masl) and a single sample with lower values in the lower part (e.g. at 23 masl). This type of heterogeneity is expected in a till deposit, where a wide range of grain size distribution coexists, as illustrated by red curves in the GSA cumulative representation (Fig. 12). The overall agreement between K-GSA and K-DCIP predictions allows further interpretation of K-DCIP distribution.

Based on Figs. 8 to 11, we could see that the reagent did not spread as expected in the TZ, with in particular a 2 m-thick “blank” section, where no conductivity changes are observed. Similar blank sections are observed in the TZ and N-S transect. This conclusion is supported by chemical monitoring, which shows that screens located in the “blank” section have a very similar chemical composition compared to before injection (Fig. 11). After the second round of injection, we see again that the reagent does not spread in this section, although the injection screens were specifically designed to fill the gap (Fig. 8, bottom row, showing ratio R9/R8). We investigate whether this behavior could have been predicted before-hand with the K-field, by comparing (i) the K-DCIP distribution before injection to (ii) the conductivity changes imaged by ERT after injection.

We plot on Fig. 13 the contours of the remediation cloud in R5 and R7 (+14 and +270 days after injection, respectively) on top of the hydraulic conductivity field (R3, before injection). Within the black contours, the formation conductivity has changed by more than 30% compared to the baseline (R3). We choose this threshold to dismiss anomalies in the range of natural variability (Fig. 8, plot showing the baseline ratio R1/R3).

In practice, we see that a major part of the reagent spreads into the less hydraulically conductive sandy till and the transition layer at 25 masl while it does not clearly spread more in the most permeable areas of the meltwater sand formation. Overall, the K-DCIP field is unable to predict injection paths and explain the reagent distribution. We conclude that, in remediation projects involving high-pressure injection, short-term spreading of the injectate is not clearly controlled by the initial K-DCIP field. While the controlling parameters of the injection paths are still under discussion, the K-DCIP field can be used for long-term estimation of contaminant mass discharge.

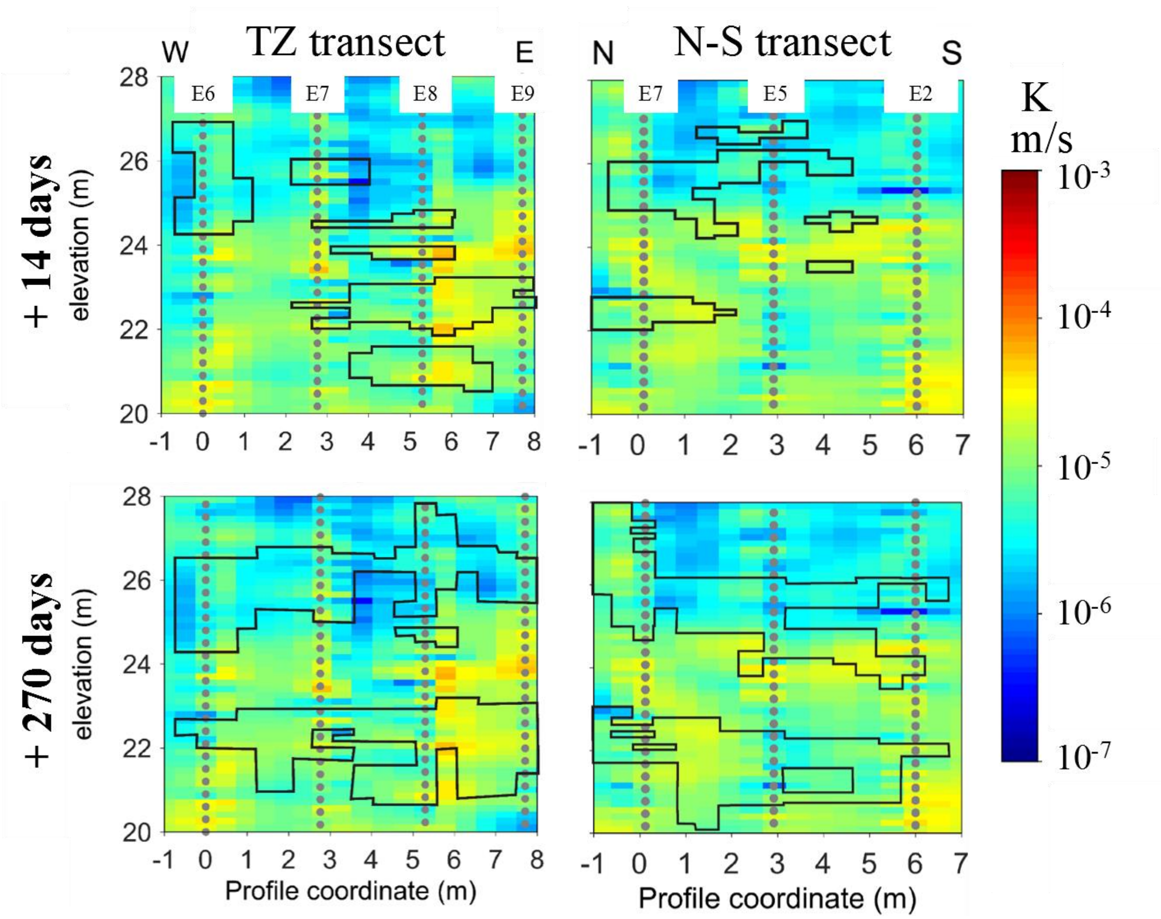

Figure 13. Overlap of the hydraulic conductivity field (background image) by the remediation cloud (area within black contour) at +14 days and +270 days. Left and right panels show the TZ and N-S transects, respectively.

Contaminant mass discharge

In the project the DCIP estimated hydraulic conductivities have been used to calculate the contaminant mass discharge. A methodology was developed to simulate the distribution of K across two control planes, downstream of a contaminated site undergoing *in situ* remediation. The results emphasized the value of a highly resolved K data set, as: i) CMD was shown to be centred around small areas of the control planes; and ii) the size of these areas was either under or overestimated, when only using slug test or GSA data. The relative uncertainty of the CMD-estimates was observed to be significantly smaller when based on IP K-estimates compared to when using slug test and GSA data. These results are reported in Thalund –Hansen et al. (2023) and in a separate note included as an appendix in Region Hovedstaden (2023), and will not be further discussed here.

Overall, this study supports that more reliable CMD-estimates can be obtained by using the IP-inferred K in addition to slug test and/or GSA K-estimates. For risk assessment and management of contaminated sites as well as for evaluation of remediation performance, this is a promising result.

5. DISCUSSION AND PERSPECTIVES

Data quality degradation

Over time, it is clear that the DCIP data quality decreases (Table 1), and there are multiple reasons for this. Firstly, we suspect that some ZVI is creating short circuits between our electrodes. Indeed, we obtained good data quality in borehole E7 during R8 (new baseline) and problematic data during R9 (after second injection), while daylighting was observed through E7 during the second injection. In addition, our surface connectors are getting worn and possibly damaged and the full contact with the instrument is not guaranteed anymore. We see scaling all around the connectors (Fig. 14). We also have to use more and more strength to open the holes (they get really stuck probably due to corrosion), which might have caused additional damage to the cables. As a result, the data quality is getting worse (unstable voltage, see Fig. 15) and we have to remove more and more datapoints to be able to reach a meaningful convergence in the inversion.

Figure 14. Pictures of the installation at round 10, showing degradation of the connectors (due to scaling and brutal opening) as well as well-head.

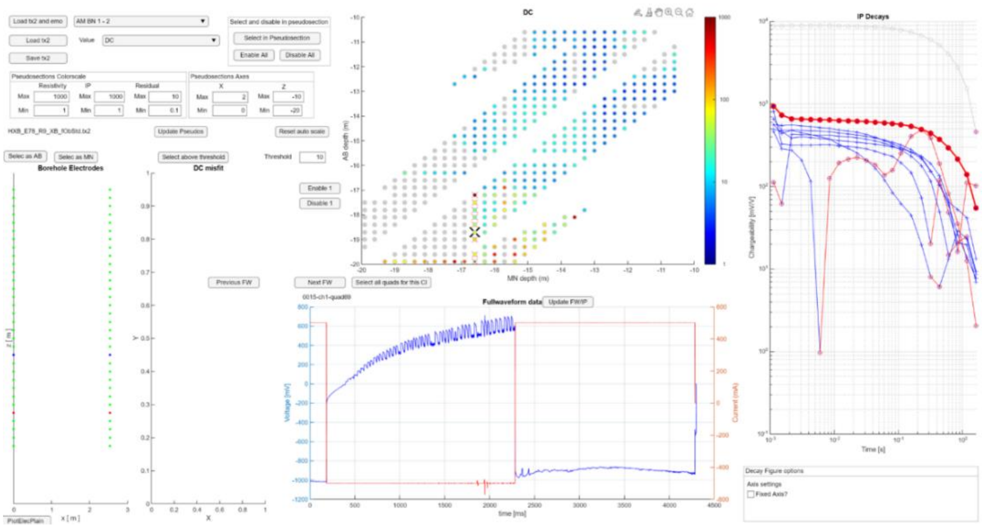

Figure 15. Illustration of poor data quality for the boreholes E7-E8 at round 9 (config. AM-BN). The bottom plot shows the fullwaveform data: current in red, relatively stable; voltage in blue, not stable).

We illustrate the consequences of this problem on the resistivity inversion results at round 10. Resistivity ratios at round 10 (last round of measurements in September 2021) are shown in Fig. 16 for the TZ and N-S transects. Two different ratios are shown: ratio of round 10 / round 8 (bottom row) and of round 10 / round 3 (top row). That way we can assess the effect of the second injection alone or of both injections together, respectively. For this round, further interpretation requires an assessment of the resolution of the inversion model, given the loss of data quality. Areas with limited sensitivity have been shaded by a white/transparent box on the transect, based on manual inspection of the data quantity and quality.

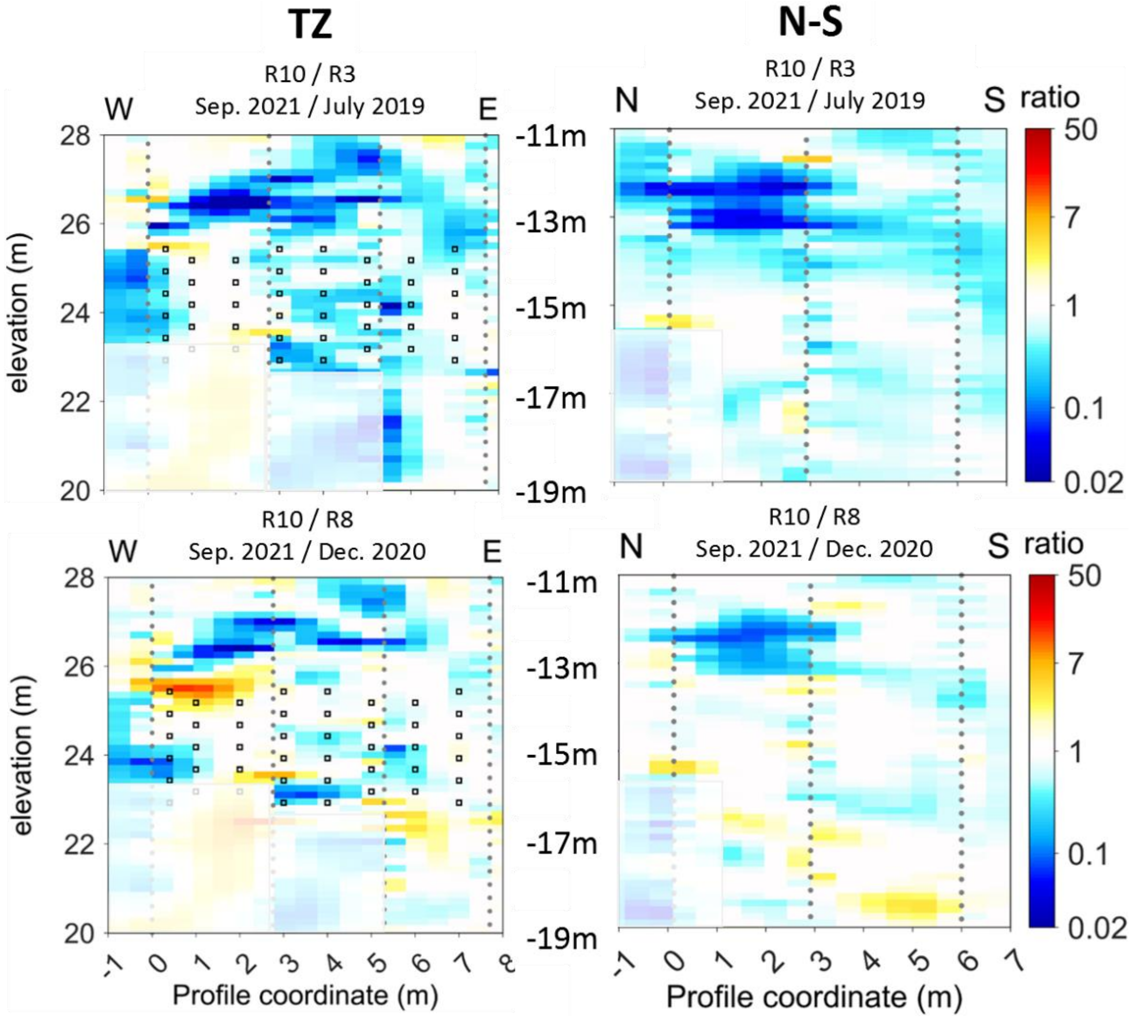

Figure 16. Cross-borehole resistivity ratio plots for round 10, at the TZ and N-S transects, including qualitative shading of the poorly resolved model cells (transparent colors). Top and bottom rows show ratios to round 3 (first baseline) and round 8 (second baseline), respectively. Injection screens for the second injection are shown on the TZ transect.

Fig. 17 shows how much data is removed in the sub-set E6-E7 for the TZ transect in round 10 (grey data are measured but removed due to poor quality, as illustrated in Fig. 15). The black rectangle on Fig. 17 shows where data or data fit is lacking in all the configuration for resolving the area between E6 and E7. We see that we are not able to retrieve meaningful information below 16 mbgs. Therefore, we add a qualitative shading on the inversion results for the TZ between E6 and E7, below 16mbgs (Fig. 16). This also includes the area around E6 since the single borehole data is also poorly resolved in this depth range. The same methodology is applied to E7-E8, resulting in a shading below 16.5m. Fortunately, good data is still retrieved for all the sub-datasets involving E9 and therefore the rest of the inversion transect is considered sufficiently resolved. The data quality over the transect E752 (N-S) is overall better. A better misfit is also achieved with the inversion, although the single borehole data of E7 has the same poor quality as in E6-E7-E8-E9.

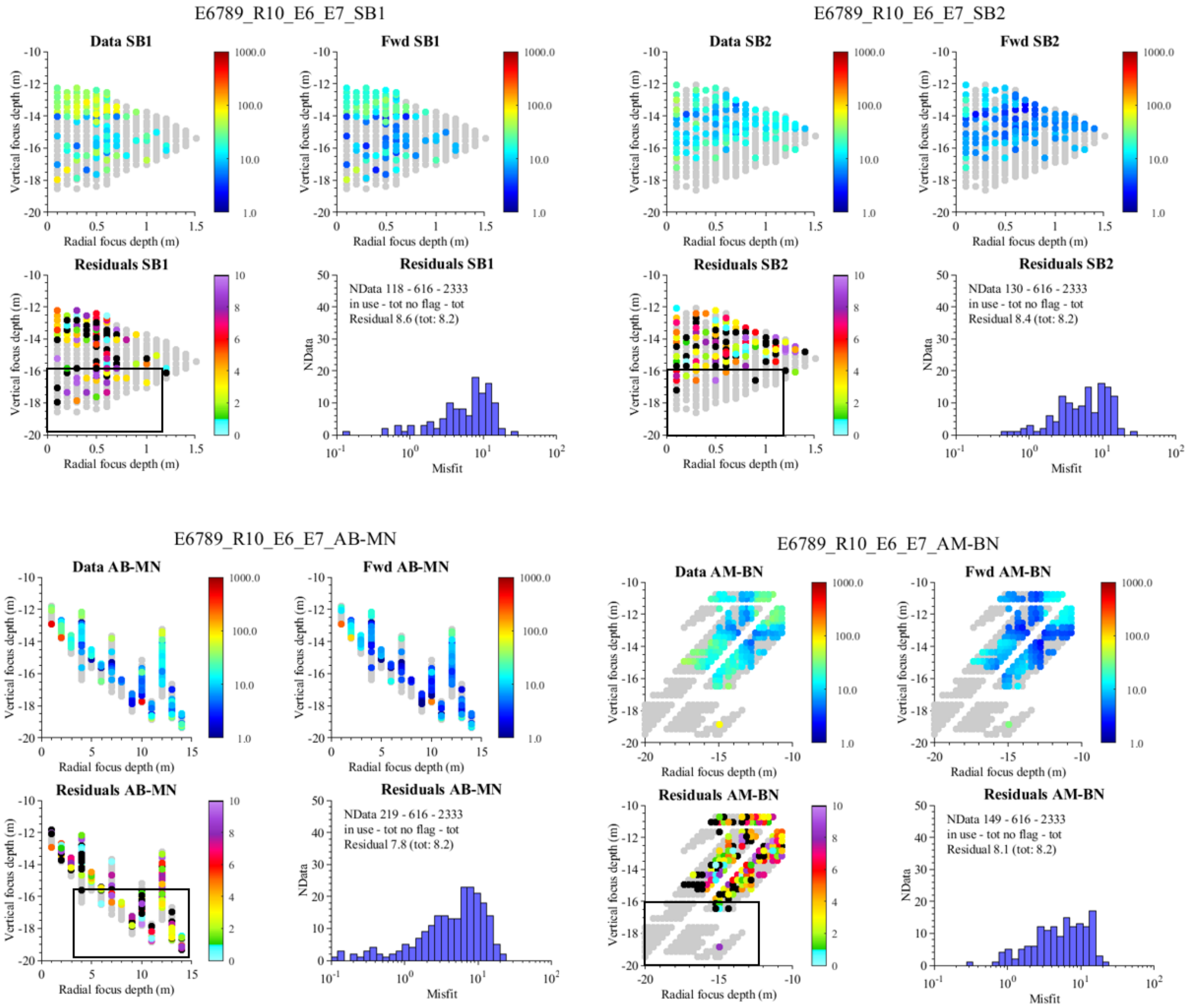

Figure 17. Pseudo-sections for the sub-dataset E6-E7 within the whole dataset E6-E7-E8-E9 at round 10. The four type of data are shown separately: SB1 (E6), SB2 (E7), AB-MN and AM-BN. Each type of data has four plots: the data, forward and residual pseudosections, as well as a histogram showing the misfit distribution. The grey circles correspond to data removed during the processing due to poor quality. The black rectangles emphasize the areas with no data or only high-misfit data. These areas result in poor resolution of the inversion.

Challenges with current field setup

The electrode boreholes installed in Hvedemarken involved steel ring electrodes mounted manually on a "Rotek" standard pipe. Each electrode is soldered manually to a wire and run up to the surface along the pipe. Obviously, this is a man-power intense process, and thereby also expensive. On the other hand, it is a solid construction that once installed could function for a long time. Though, as described above, there are issues connected to the connections linking the electrode tube with the instruments through a connector. These connectors visibly wear over time and are prone to damage under rough handling. Better protection should therefore be considered.

Once the electrode pipes are constructed, they are installed on the inside of a borehole stem while retracting. The installation on the inside of the drilling equipment involves a risk of damaging the electrodes and cables that are running on the outside of the electrode pipes.

Finally, the electrode pipes are constructed in fixed lengths ideally matching the drilling equipment for easier installation. The wires are mounted across the fixed stems so that the entire length of electrode pipes can be transported in a folded manner. Though, due to the stiff pipe pieces, the installation is still complicated although doable.

Improvements for the field setup

In a parallel project funded by Innovation Fund Denmark (GiRem), the company Ejlskov investigated several options for improving the construction of the borehole electrodes and the installation process. In the end, they suggested electrodes mounted on a 32-wire flat ribbon cable. Each of the 32 wires is connected by soldering to a large steel electrode. This construction allows the entire electrode cable to be wound up for easy transport. Installation is inside a drilling stem with a small weight at the end to keep it straight. In this manner both the material consumption, the construction, and the installation have been improved significantly using standard direct push drilling rigs.

One of the main issues with electrode installation in the ground is to ensure a good connection between the electrodes and the surrounding soil. Depending on the dimensions of the drilling equipment, the lithologies at the site and other considerations, the hole with the electrodes installed is often backfilled with some material to pack it up. In Hvedemarken, the holes were backfilled with sand, whereas the approach in GiRem has been to backfill with a bentonite-cement slurry, which has been tuned to ensure a good contact to the electrodes and ensuring the integrity of the hole over time. The added costs for this backfilling is estimated to be small. The bentonite-cement backfill seems to minimize the so-called *borehole effects,* which are normally a very tricky part of the inversion fine-tuning as will be briefly discussed below.

The entire process of electrode manufacturing and installation was in GiRem taken care of by Ejlskov with the University in an advisory role only.

The other big improvement on the hardware side, is the development in GiRem of a full 3D DCIP instrument tailored for cross-borehole applications. The instrument is referred to as Adapt and can collect high-quality data in a full 3D setup, meaning that one can inject current in one borehole and then obtain voltage potentials from up to 9 other boreholes each with 32 electrodes. What this means is that the data collection can collect 10 times more data in less time than the system used in Hvedemarken. A rough estimate suggests that the Hvedemarken setup could be measured within maybe two hours but acquiring around 10 times more data in full 3D. This instrument is fully functional and relatively easy to operate, but so far only available through Aarhus University.

Challenges in current data processing and inversion

The dataflow involves first processing for noise and bad data and after that the data are inverted for a subsurface parameter model.

In the early phases of the Hvedemarken project, the data processing was almost entirely manual, which means that every single measurement is manually inspected and kept or discarded. This process delivers data of very high quality, but it is also very time-consuming. In the context of GiRem, an automated process was developed, which involved an automatic processing step where each individual measurement is flagged good/bad. The auted process is based on a simple modelling step where it is checked if the current dataset is reproducible by a physical model. If not, then the dataset is flagged as bad. This process has been applied to most of the data in Hvedemarken and has proven to be very useful.

The numerical computation in the inversion of the data is handled by the code AarhusInv. The communication with AarhusInv is carried out by several Matlab-scripts writing the input files in the correct formats and reading and plotting the output from the code. This is not user-friendly and requires expert knowledge as it is today. There are not today any user-interface programs that can handle data in the amounts and types produced in a case-study like Hvedemarken.

A final remark on the current stage of the data processing and inversion involves challenges in the fine-tuning of inversion and specially handling what is referred to as *borehole effects*. Setting and fine-tuning the parameters for the inversion can be quite tricky and involves a relatively high degree of trial-and-error including expert knowledge. *Borehole effects* is a particular challenge in the fine-tuning and it is quite evident in the results presented here, although a lot of effort has been put in minimizing it.

Improvements in data processing

Today, the automatic processing mentioned above is a tool that can be easily used, but it is currently only implemented using Matlab and there is therefore a need to implement it in a more user-friendly software to enable it for more users.

The inversion part also lacks a user-friendly tool or software that can bring the use to a larger group of people. The AarhusWorkbench uses the AarhusInv code as a backbone for all the other geophysical data being collected in Denmark and elsewhere such as SkyTEM, tTEM, and ERT. It would therefore be relatively easy to include cross-borehole data into this software, but the question is if the commercial market is big enough for this to be profitable for Aarhus Geosoftware/Seequent who develops the software.

Last thing worth mentioning is the continued efforts to build inversion tools in 3D. In the GiRem project Aarhus University has developed a 3D inversion code for cross-borehole data. At this point the code only supports DC (or resistivity) inversions, but the plan is to expand it to include IP as well. The main strength of the code is that it has greatly reduced the computation times needed for 3D inversions, while maintaining a very high grid density allowing to resolve small features. Similar to the comments above the program does not have a user-interface and it is also on a slightly more primitive stage than the processing and inversion tools mentioned above.

6. CROSS BOREHOLE DCIP FOR MONITORING OF REMEDIAL ACTIONS?

The DCIP method can contribute to monitoring of remedial action with respect to three aspects:

- Monitoring the injection by use of cross-borehole ERT
- Determination of hydraulic conductivity from DCIP data
- Quantification of Contaminant Mass Discharge (CMD)

Resistivity variations measured by cross-borehole ERT provide a visualization tool for the spatial and temporal distribution of ZVI reagent spreading at Hvedemarken remediation site. The injection of Provect-IR® reagent, containing 45% of mZVI, leads to the release of ionic species, including Ca^{2+}, HCO_3^- and Fe^{2+}/Fe^{3+}, which causes a significant increase of water EC at places where the product migrates. The ERT-inferred distribution is consistent with chemical monitoring, while providing a more complete image of the remediation cloud spatial distribution. On the other hand, water and sediment samples are still needed for discriminating different species and understanding on-going chemical reactions.

The value of the method for monitoring of the injection cloud is well documented in this study. The advantage in the high-resolution picture of the spatial distribution. This provided a rapid, spatially continuous, and well-resolved assessment of the reagent distribution. In combination with 1-2 traditional monitoring rounds this can form the basis for reinjection in specific areas. The result in this study supports that the DCIP provides a reliable spreading of the injection cloud in the treatment zone. It is recommended to a higher degree to include level specific water sampling in order to do a point to point comparison of the DCIP and groundwater sampling.

Compared to surface ERT, cross-borehole ERT offers significantly more flexibility and better spatial resolution in the depth-range of interest. It is particularly suitable for urban areas where limited space is available for laying out surface electrodes.

In the context of high-pressure injection, where daylighting is likely to happen, cross-borehole ERT monitoring upstream and above the injection would have an additional value to rapidly assess unexpected and problematic flow-paths.

The geoelectrical cross-borehole induced polarization (IP) data collected at the site made it possible to determining 2D hydraulic conductivity (K) distributions with an inversion model resolution of 0.15 m (vertically) x 0.50 m (horizontally) in three control planes from 10-20 m depth. The geometric means and variance of the IP, slug test, and GSA derived K-estimates were consistent.

Slug test and GSA are well established and accepted methods for field/lab estimation of K applied by scientists and practitioners. For the cross-borehole IP K-method to gain the same confidence and applicability, it still needs to be improved. First of all, the empirical relation applied for K-estimation (Eq. 4) needs more laboratory testing with sediments from different geological settings. The field comparison between K-values in the sandy till in this study is limited as very few screens are placed in this part of the aquifer.. The empirical relation has shown applicability in our study and in these studies without further calibration, but there is a need for further field testing to ensure applicability in geological settings of different nature.

Overall, this study supports that more reliable CMD-estimates can be obtained by using the IP-inferred K in addition to slug test and/or GSA K-estimates. For risk assessment and management of contaminated sites as well as for evaluation of remediation performance, this is a promising result.

Finally it should be noted that in particular IP data has been suggested as useful for monitoring long term performance of remedial actions and geochemical changes (Kessouri et al., 2022). This has been tested in the final phases of the project, however, the work is so far inconclusive. The IP data provides interesting patterns, but strong relationship with changes in water chemistry or geochemical processes have not established (Thalund-Hansen et al. in prep). Future investigations of the IP response of ZVI particles in the field might reveal additional potential of the method to distinguish the ionic cloud from ZVI particles.

REFERENCES

Archie, G. E. (1942), The electrical resistivity log as an aid in determining some reservoir characteristics, *Transactions of the AIME*, *146*(01), 54-62.

Auken, E., et al. (2014), An overview of a highly versatile forward and stable inverse algorithm for airborne, ground-based and borehole electromagnetic and electric data, *Explor. Geophys*, 1-13.

Balbarini, N., P. K. Maurya, V. Rønde, G. Fiandaca, I. Møller, K. E. S. Klint, A. V. Christiansen, P. J. Binning, and P. L. Bjerg (2018), Geophysics based contaminant mass discharge quantification downgradient of a landfill and a former pharmaceutical factory, *Water Resources Research*, *8*(54), 436-5456.

Bertin, J., and J. Loeb (1976), *Experimental and Theoretical aspects of induced polarization, Vol. 1*, Schweizerbart Science Publishers.

Bing, Z., and S. Greenhalgh (2001), Cross-hole resistivity tomography using different electrode configurations, *Geophysical prospecting*, *48*(5), 887-912.

Binley, A., J. Keery, L. Slater, W. Barrash, and M. Cardiff (2016), The hydrogeologic information in cross-borehole complex conductivity data from an unconsolidated conglomeratic sedimentary aquifer, *Geophysics*, *81*(6), E409-E421.

Bording, T., A. K. Kühl, G. Fiandaca, J. F. Christensen, A. V. Christiansen, and E. Auken (2021), Cross-borehole geoelectrical time-lapse monitoring of in situ chemical oxidation and permeability estimation through induced polarization, *Near Surface Geophysics*, *19*(1), 43-58.

Bording, T., G. Fiandaca, P. K. Maurya, E. Auken, A. V. Christiansen, N. Tuxen, K. E. S. Klint, and T. H. Larsen (2019), Cross-borehole tomography with full-decay spectral time-domain induced polarization for mapping of potential contaminant flow-paths, *Journal of contaminant hydrology*, *226*, 103523.

Bücker, M., and A. Hördt (2013), Analytical modelling of membrane polarization with explicit parametrization of pore radii and the electrical double layer, *Geophysical Journal International*, *194*(2), 804-813.
Cole, K. S., and R. H. Cole (1941), Dispersion and absorption in dielectrics. I. Alternating current characteristics, *J. Chem. Phys.*, *9*, 341-351.
Daily, W., and A. Ramirez (1995), Electrical resistance tomography during in-situ trichloroethylene remediation at the Savannah River Site, *Journal of Applied Geophysics*, *33*(4), 239-249.
Fiandaca, G., L. M. Madsen, and P. K. Maurya (2018a), Re-parameterisations of the Cole--Cole model for improved spectral inversion of induced polarization data, *Near Surface Geophysics*, *16*(4), 385-399.
Fiandaca, G., J. Doetsch, G. Vignoli, and E. Auken (2015), Generalized focusing of time-lapse changes with applications to direct current and time-domain induced polarization inversions, *Geophysical Journal International*, *203*(2), 1101-1112.
Fiandaca, G., J. Ramm, A. Binley, A. Gazoty, A. V. Christiansen, and E. Auken (2013), Resolving spectral information from time domain induced polarization data through 2-D inversion, *Geophysical Journal International*, *192*, 631-646.
Fiandaca, G., P. K. Maurya, N. Balbarini, A. Hördt, A. V. Christiansen, N. Foged, P. L. Bjerg, and E. Auken (2018b), Permeability estimation directly from logging-while-drilling Induced Polarization data, *Water Resources Research*, *54*(4), 2851-2870.
Flores Orozco, A., V. Micić, M. Bücker, J. Gallistl, T. Hofmann, and F. Nguyen (2019), Complex-conductivity monitoring to delineate aquifer pore clogging during nanoparticles injection, *Geophysical Journal International*, *218*(3), 1838-1852.
Flores Orozco, A., M. Velimirovic, T. Tosco, A. Kemna, H. Sapion, N. Klaas, R. Sethi, and L. Bastiaens (2015), Monitoring the injection of microscale zerovalent iron particles for groundwater remediation by means of complex electrical conductivity imaging, *Environmental Science & Technology*, *49*(9), 5593-5600.
Joyce, R. A., D. R. Glaser Ii, D. D. Werkema Jr, and E. A. Atekwana (2012), Spectral induced polarization response to nanoparticles in a saturated sand matrix, *Journal of applied geophysics*, *77*, 63-71.
Kessouri, P., Johnson, T., Day-Lewis, F. D., Wang, C., Ntarlagiannis, D., & Slater, L. D. (2022). Post remediation geophysical assessment: Investigating long-term electrical geophysical signatures resulting from bioremediation at a chlorinated solvent contaminated site. *Journal of Environmental Management*, *302*(PA), 113944. https://doi.org/10.1016/j.jenvman.2021.113944
LaBrecque, D. J., A. L. Ramirez, W. D. Daily, A. M. Binley, and S. A. Schima (1996), ERT monitoring of environmental remediation processes, *Measurement Science and Technology*, *7*(3), 375.
Lévy, L., B. Gibert, F. Sigmundsson, F. Parat, D. Deldicque, and G. P. Hersir (2019a), Tracking magmatic hydrogen sulphur circulations using electrical impedance : complex electrical properties of core samples at the Krafla volcano, Iceland, *Journal of Geophysical Research: Solid Earth*, *124*(3), 2492-2509.
Lévy, L., B. Gibert, F. Sigmundsson, Ó. G. Flóvenz, G. P. Hersir, P. Briole, and P. A. Pezard (2018), The role of smectites in the electrical conductivity of active hydrothermal systems: electrical properties of core samples from Krafla volcano, Iceland, *Geophysical Journal International*, *215*(3), 1558-1582.
Lévy, L., P. K. Maurya, S. Byrdina, J. Vandemeulebrouck, F. Sigmundsson, K. Arnason, and e. al. (2019b), Electrical Resistivity Tomography and Time-Domain Induced Polarization field investigations of geothermal areas at Krafla, Iceland: comparison to borehole and laboratory frequency-domain electrical observations, *Geophysical Journal International*.
Lévy, L., R. Thalund-Hansen, T. Bording, G. Fiandaca, A. V. Christiansen, K. Rügge, N. Tuxen, M. Hag, and P. L. Bjerg (accepted), Quantifying reagent spreading by cross borehole electrical tomography to assess the performance of contaminated aquifers remediation, *Water Resources Research*.
Loke, M. H., and R. D. Barker (1996), Rapid least squares inversion of apparent resistivity pseudosections by a quasi-Newton method, *Geophysical Prospecting*, *44*, 131-152.
Maurya, P. K., N. Balbarini, I. Møller, V. Rønde, A. V. Christiansen, P. L. Bjerg, E. Auken, and G. Fiandaca (2018a), Subsurface imaging of water electrical conductivity, hydraulic permeability and lithology at contaminated sites by induced polarization, *Geophysical Journal International*, *213*(2), 770-785.

Maurya, P. K., N. Balbarini, I. Møller, V. Rønde, A. V. Christiansen, P. L. Bjerg, E. Auken, and G. Fiandaca (2018b), Subsurface imaging of water electrical conductivity, hydraulic permeability and lithology at contaminated sites by induced polarization, *Geophysical Journal International*(213), 770 - 785.
Nivorlis, A., M. Rossi, and T. Dahlin (2021), Temporal filtering and time-lapse inversion of geoelectrical data for long-term monitoring with application to a chlorinated hydrocarbon contaminated site, *Geophysical Journal International*.
Nivorlis, A., T. Dahlin, M. Rossi, N. Höglund, and C. Sparrenbom (2019), Multidisciplinary characterization of chlorinated solvents contamination and in-situ remediation with the use of the direct current resistivity and time-domain induced polarization tomography, *Geosciences*, *9*(12), 487.
Pelton, W. H., S. H. Ward, P. G. Hallof, W. R. Sill, and P. H. Nelson (1978), Mineral discrimination and removal of inductive coupling with multifrequency IP, *Geophysics*, *43*(3), 588-609.
Phenrat, T., H.-J. Kim, F. Fagerlund, T. Illangasekare, R. D. Tilton, and G. V. Lowry (2009), Particle size distribution, concentration, and magnetic attraction affect transport of polymer-modified Fe0 nanoparticles in sand columns, *Environmental science & technology*, *43*(13), 5079-5085.
Pridmore, D. F., and R. T. Shuey (1976), The electrical resistivity of galena, pyrite, and chalcopyrite, *American Mineralogist*, *61*(3-4), 248-259.
Revil, A., M. F. Sleevi, and D. Mao (2017), Induced polarization response of porous media with metallic particles--Part 5: Influence of the background polarization, *Geophysics*, *82*(2), E77-E96.
Region Hovedstaden (2023). Hvedemarken 3-5, Farum. Innovative ZVI application for plume remediation. Monitoring 36 months after creation of PRB. (21 months after reinjection). Report by COWI May 2023.
Robinson, J., L. Slater, A. Weller, K. Keating, T. Robinson, C. Rose, and B. Parker (2018), On permeability prediction from complex conductivity measurements using polarization magnitude and relaxation time, *Water Resources Research*, *54*(5), 3436-3452.
Shi, Z., D. Fan, R. L. Johnson, P. G. Tratnyek, J. T. Nurmi, Y. Wu, and K. H. Williams (2015), Methods for characterizing the fate and effects of nano zerovalent iron during groundwater remediation, *Journal of Contaminant Hydrology*, *181*, 17-35.
Shuey, R. T. (1975), *Semiconducting ore minerals*, Elsevier Scientific Publishing Company Amsterdam.
Singha, K., and S. M. Gorelick (2005), Saline tracer visualized with three-dimensional electrical resistivity tomography: Field-scale spatial moment analysis, *Water Resources Research*, *41*(5).
Slater, L., J. Choi, and Y. Wu (2005), Electrical properties of iron-sand columns: Implications for induced polarization investigation and performance monitoring of iron-wall barriers, *Geophysics*, *70*(4), G87-G94.
Slater, L., D. Ntarlagiannis, and D. Wishart (2006), On the relationship between induced polarization and surface area in metal-sand and clay-sand mixtures, *Geophysics*, *71*(2), A1-A5.
Slater, L., A. Binley, R. Versteeg, G. Cassiani, R. Birken, and S. Sandberg (2002), A 3D ERT study of solute transport in a large experimental tank, *Journal of applied geophysics*, *49*(4), 211-229.
Sumner, J. S. (1976), Principles of induced polarization for geophysical exploration, in *Developments in economic geology*, *5*, edited, Elsevier Scientific Publishing Company Amsterdam.
Telford, W. M., L. P. Geldart, and R. E. Sheriff (1990), *Applied Geophysics*, Cambridge University Press.
Thalund-Hansen, R.; Troldborg, M., Levy, L.; Christiansen, A.V.; Bording, T.S.; Bjerg, P.L. (2023). Assessing contaminant mass discharge uncertainty with application of hydraulic conductivites from geoelectrical cross-borehole induced polarization and other methods, Water Resources Research, under revision.
Thalund-Hansen, R.; M., Levy, L.; Rügge, K.; Dreyer, M., Christiansen, A.V., Tuxen, N.; Hag, M..; Bjerg, P.L. (2023). Assessing the performance of in situ remediation by relating biogeochemical processes to cross-borehole DCIP measurements. In preparation.
Velimirovic, M., T. Tosco, M. Uyttebroek, M. Luna, F. Gastone, C. De Boer, N. Klaas, H. Sapion, H. Eisenmann, and P.-O. Larsson (2014), Field assessment of guar gum stabilized microscale zerovalent iron particles for in-situ remediation of 1, 1, 1-trichloroethane, *Journal of contaminant hydrology*, *164*, 88-99.
Waxman, M. H., and L. J. M. Smits (1968), Electrical conductivities in oil-bearing shaly sands, *Soc. Pet. Eng. J.*, *8*, 107-122.

Weller, A., and L. Slater (2019), Permeability estimation from induced polarization: an evaluation of geophysical length scales using an effective hydraulic radius concept, *Near Surface Geophysics*, *17*(6), 581-594.

Weller, A., L. Slater, and S. Nordsiek (2013), On the relationship between induced polarization and surface conductivity: Implications for petrophysical interpretation of electrical measurements, *GEOPHYSICS*, *78*(5), D315-D325.

Weller, A., L. Slater, A. Binley, S. Nordsiek, and S. Xu (2015), Permeability prediction based on induced polarization: Insights from measurements on sandstone and unconsolidated samples spanning a wide permeability range, *Geophysics*, *80*(2), D161-D173.